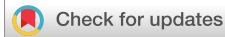


RESEARCH ARTICLE | MAY 08 2025

# Quasi-perfect spiral sound-absorbing metasurfaces for ultra-broadband motor vibration and noise reduction

Huilan Wu ; Han Zhang ; Yijun Liu  

AIP Advances 15, 055216 (2025)

<https://doi.org/10.1063/5.0271926>

## Articles You May Be Interested In

Acoustic perfect absorbers via spiral metasurfaces with embedded apertures

*Appl. Phys. Lett.* (December 2018)

A compact low-frequency sound-absorbing metasurface constructed by resonator with embedded spiral neck

*Appl. Phys. Lett.* (November 2020)

Underwater broadband sound insulation with chiral spiral structures

*AIP Advances* (December 2020)



## Special Topics Open for Submissions

[Learn More](#)

# Quasi-perfect spiral sound-absorbing metasurfaces for ultra-broadband motor vibration and noise reduction

Cite as: AIP Advances 15, 055216 (2025); doi: 10.1063/5.0271926

Submitted: 20 March 2025 • Accepted: 25 April 2025 •

Published Online: 8 May 2025



View Online



Export Citation



CrossMark

Huilan Wu,<sup>1</sup>  Han Zhang,<sup>2,a)</sup>  and Yijun Liu<sup>1,a)</sup> 

## AFFILIATIONS

<sup>1</sup> Department of Mechanics and Aerospace Engineering, Southern University of Science and Technology, Shenzhen 518055, Guangdong, China

<sup>2</sup> Laboratory of Noise and Audio Research, Institute of Acoustics, Chinese Academy of Sciences, Beijing 100190, China

<sup>a)</sup> Authors to whom correspondence should be addressed: [zhanghan@mail.ioa.ac.cn](mailto:zhanghan@mail.ioa.ac.cn) and [liuyj3@sustech.edu.cn](mailto:liuyj3@sustech.edu.cn)

## ABSTRACT

Effectively reducing motor vibration and radiated noise is a highly challenging technical problem, especially under complex multi-physics coupling conditions. This paper proposes a novel design strategy involving a rubber-embedded quasi-perfect spiral acoustic metasurface to effectively reduce motor vibration and radiated noise. When the spiral metasurface is combined with rubber, it is equivalent to a mass-spring system. When the motor's vibration frequency matches the natural frequency of the structure, the system undergoes resonant absorption, significantly reducing the vibration amplitude. Simultaneously, the spiral metasurface can redistribute the phase of sound waves and extend the sound wave path, causing opposite response modes on the upper and lower surfaces, achieving complete sound absorption at specific frequencies. This method is not affected by the motor's operating conditions and can achieve vibration and noise reduction in specific frequency bands by adjusting parameters such as spiral path length, order, and rubber thickness. The structure's thickness is only one-tenth of the motor's diameter. Numerical results show that embedding just two spiral metasurfaces in the damping rubber can reduce the radiated noise by an average of 6 dB, decrease the relative vibration amplitude peak by 0.99, and achieve a frequency band attenuation rate of over 80%. This method provides a new solution for ultra-broadband vibration and noise reduction in motors and lays the foundation for similar designs in complex rotating machinery.

© 2025 Author(s). All article content, except where otherwise noted, is licensed under a Creative Commons Attribution-NonCommercial-NoDeriv 4.0 International (CC BY-NC-ND) license (<https://creativecommons.org/licenses/by-nc-nd/4.0/>). <https://doi.org/10.1063/5.0271926>

## I. INTRODUCTION

Motors are extensively employed in propulsion systems within the aerospace sector and other industries. They drive aircraft flight and support the normal operation of various equipment, playing an essential role in the development of aerospace technology. As technology advances, modern motors face increasingly stringent requirements regarding weight and volume. Enhanced power density and energy density are critical for achieving the lightweight and compact designs demanded by contemporary aerospace applications.<sup>1</sup> Vibration and noise are inherent issues during motor operation,<sup>2</sup> which can adversely affect motor performance and stability. Implementing vibration and noise reduction technologies can enhance the motor's operational efficiency, accuracy, and

reliability, thereby improving the overall quality and performance of the product.<sup>3</sup>

Traditional methods for reducing motor vibration and noise primarily involve structural design,<sup>4,5</sup> material selection,<sup>6,7</sup> and control strategies.<sup>8–10</sup> In 2002, researchers published pioneering work on mechanical vibration and noise control in motor systems, offering valuable references for advancing motor vibration and noise control techniques.<sup>4</sup> Zou *et al.* optimized the slot width of the motor rotor to reduce the magnetic amplitude near the resonance frequency.<sup>11</sup> Sun *et al.* investigated the impact of pole slot combinations on the vibration and noise of permanent magnet synchronous motors.<sup>12</sup> Wang and Li proposed an improved rotor structure incorporating an auxiliary flux barrier to reduce radial electromagnetic forces, thereby attenuating electromagnetic vibration and noise.<sup>13</sup>

However, as motor performance advances, the conditions for vibration and noise become increasingly complex, rendering traditional reduction methods insufficient to meet current demands. First, while many studies effectively reduce motor vibration and noise, they often significantly weaken the output torque.<sup>14</sup> Second, previous optimization methods necessitate different approaches for different motors, which increases manufacturing costs and processing complexity. Consequently, there remains a lack of a universal method for vibration and noise reduction.

In recent years, novel acoustic metasurfaces have emerged as effective tools for controlling and reducing noise by manipulating the propagation and scattering of sound waves through precisely engineered microstructures.<sup>15–19</sup> Compared to traditional acoustic materials, acoustic metasurfaces offer superior noise control across a broader frequency range, with enhanced performance from low to high frequencies.<sup>20–22</sup> The microstructure of acoustic metasurfaces can be customized and designed according to specific requirements, allowing adaptation to various application scenarios and demands.<sup>23–25</sup> The adaptability and customizable nature of acoustic metasurfaces enable optimization for various noise challenges, ensuring optimal noise control effects. Moreover, acoustic metasurfaces typically possess smaller dimensions and lighter weight,<sup>26,27</sup> facilitating effective noise control within constrained spaces.<sup>28</sup> This characteristic renders them particularly suitable for applications with limited space, such as aerospace,<sup>29</sup> automotive,<sup>30</sup> construction, and other industries.<sup>31</sup>

For instance, Liu *et al.* introduced a design methodology for a metasurface anechoic coating aimed at reducing pipeline ventilation noise. By implementing an ultra-thin labyrinth channel sound-absorbing metasurface structure on the inner wall surface of the pipeline, they achieved broadband noise reduction at low frequencies.<sup>32</sup> Meanwhile, Popa *et al.* employed highly compact active meta-atoms to construct a barrier and proposed an acoustic bianisotropic material exhibiting non-zero strain and momentum coupling. This material, not constrained by feedback stability requirements, surpassed expectations in terms of attenuation, bandwidth, and shielding volume, thus representing a cutting-edge sound isolator.<sup>33</sup> Zhou *et al.* introduced a loosely coupled reflective impedance waterborne acoustic metasurface (WAM) to attain precise control over underwater acoustics. They developed a functional-structural integrated topology optimization framework incorporating surface impedance models and vibration coupling constraints to systematically engineer WAM.<sup>34</sup> These notable advancements underline the expansive potential applications of acoustic metasurfaces in the realms of vibration and noise reduction.<sup>35</sup>

For shell structures, acoustic black hole (ABH) technology has seen significant development in recent years, with designs such as single- and double-leaf ABH configurations applied to underwater pressure-resistant shells, providing new insights into the development of potential broadband vibration and noise reduction structures.<sup>36,37</sup> Compared to such structures, the rubber-based acoustic metasurface embedded with spiral units proposed in this study has good integrability and mechanical compliance when applied to rotating machinery and can be stably installed under complex boundary conditions. It avoids complex thickness gradient design, making the manufacturing and debugging process simpler and more efficient, and is particularly suitable for vibration and noise reduction in motors and other compact rotating systems.

In previous research, we proposed a spiral-shaped quasi-perfect sound-absorbing metasurface.<sup>38</sup> This spiral metasurface exhibits a quasi-perfect sound absorption coefficient (up to nearly 0.998) and can flexibly adjust the frequency of perfect sound absorption based on parameter design.<sup>38,39</sup> It shows great potential for applications in vibration and noise reduction in small spaces. In conjunction with the technical challenges addressed in this article, such as mitigating vibration noise sources in small-sized motors, acoustic metasurfaces demonstrate promising application prospects. First, acoustic metasurfaces have the capability to achieve sub-wavelength sizes.<sup>40</sup> Second, they impose no specific material or operational condition requirements, offering flexible configuration adjustments according to specific needs. This adaptability grants them a broad applicability across diverse scenarios.

This paper designs a vibration and noise reduction covering layer with a rubber embedded spiral metasurface for the motor. By using only two spiral metasurfaces, the performance of ultra-wideband vibration reduction and quasi-perfect sound absorption is achieved. This study regards the motor and the metasurface as a whole, and the research results include the interaction between the sound field and the structure. The design fills the motor housing with damping rubber and embeds the spiral metasurface. The damping rubber is similar to a shock absorber, which first suppresses the vibration of the motor. The spiral metasurface performs broadband quasi-perfect absorption of the leaked radiated sound field, achieving dual suppression of motor vibration and noise. The structure is independent of the internal structure and operating state of the motor and has universal applicability. Moreover, the flexibility of the structure allows it to be adjusted in size according to the size of the motor, further enhancing its versatility. The design length of the spiral metasurface depends on the thickness of the rubber layer, and thinner rubber layers are preferred because they can achieve more compact structures while still maintaining excellent sound insulation and shock absorption performance. This not only improves material efficiency but also helps reduce weight, making the structure lightweight, efficient, and highly adaptable to practical engineering applications.

## II. DESIGN CONCEPT

The spiral structure originally discovered in the biological world constitutes an asymmetric structure, such as snail shells and DNA structures, which is characterized by the fact that neither single nor double helices are completely symmetrical. In this study, we use single helical paths to form elastic metasurface structures and systematically study their core mechanisms and acoustic behaviors. Specifically, we embed the spiral metasurface into rubber and apply it to the surface of the motor. It is worth noting that in actual motor applications, the vibration of the motor cannot be ignored, so the sound absorption performance of the spiral periodic structure alone is significantly different from that when the influence of motor vibration is considered. In order to show this difference, we briefly introduce the sound absorption performance and theoretical mechanism of the spiral periodic metasurface when it acts alone in this section. Sections III–VI will discuss the motor vibration reduction and noise reduction in detail.

Figure 1 illustrates the overall concept of the vibration and noise reduction structure design: a damping rubber structure with

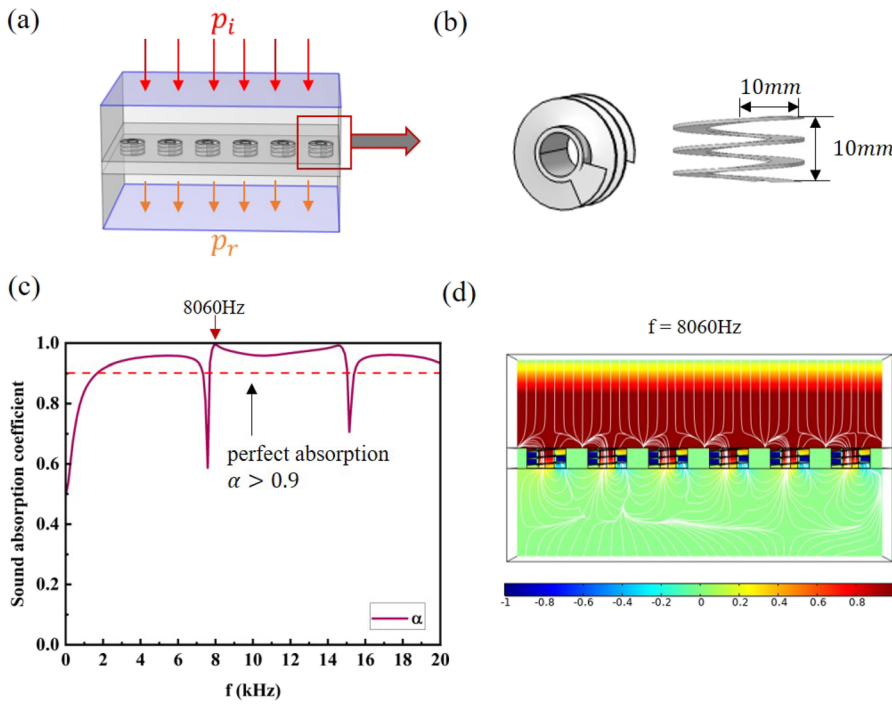


**FIG. 1.** Model diagram of periodic helical metasurfaces and calculation results of sound absorption efficiency: (a) schematic diagram of periodic helical metasurfaces placed in a waveguide, (b) schematic diagram of the internal structure of helical metasurface unit, (c) absorption coefficient curve of periodic helical metasurfaces, and (d) sectional view of the sound pressure distribution at the absorption peak frequency.

periodic spiral metasurfaces. To facilitate understanding, we first present its tiled configuration, as shown in Fig. 1(a). The core of each spiral unit comprises a hollow cylinder, surrounded by a spiral path. The periodic structure is based on damping rubber, with the spiral metasurface positioned within six circular holes along the central axis. The entire periodic structure is placed in a rectangular waveguide, with radiation boundary conditions applied at both ends, with one end serving as the incident plane wave boundary. The incident sound wave  $p_i$  is a plane wave incident from the upper end, and  $p_r$  is the transmitted sound wave. The sound wave attenuation coefficient is calculated using  $\alpha = 1 - |p_r/p_i|$ .

Figure 1(b) presents a schematic diagram of the internal structure of the spiral metasurface, with a radius of 10 mm and a thickness of 10 mm. Figure 1(c) displays the sound attenuation coefficient of the spiral metasurface periodic structure, calculated across the frequency range of 20–20 kHz. As illustrated in the figure, the sound attenuation coefficient of this structure exceeds 0.5, indicating that at least 50% of the sound pressure is attenuated. A perfect sound absorption coefficient is defined as  $\alpha > 0.9$ . The results demonstrate that 90% of the sound waves in the target frequency band achieve perfect sound absorption, validating the ultra-broadband sound absorption characteristics of this structure. Figure 1(d) illustrates the sound pressure distribution at the sound absorption peak. It is evident from the figure that the sound wave at the incident end is nearly entirely absorbed by the spiral metasurface. Then, the sound wave undergoes multiple refractions and reflections within the spiral unit until the energy leakage at the exit end is minimized, thereby achieving perfect sound wave attenuation.

Since the spiral unit is on the sub-wavelength scale, it can be regarded as a mean unit. According to effective medium theory,

the surface properties of the mean unit can be characterized by its Green's function,<sup>41</sup>

$$G_i(r, r') = \sum_n c_n \psi_n(r) \psi_n^*(r'). \quad (1)$$

Here,  $G(r, r')$  is the Green's function, which describes the effect of the excitation at position  $r$  on the response at position  $r'$ .  $\psi_n(r)$  is the  $n$ th eigenfunction of the element.  $c_n$  is the expansion coefficient used to represent the contribution of each eigenfunction to the overall Green's function. The following is a detailed derivation.

The scattered field  $\psi_{sc}$  on the boundary surface  $\partial s$  is related to its eigenfunction  $\psi_n$  as follows:

$$\psi_{sc}(x') = \oint_{\partial s} G_m(x', \zeta) \psi_n(\zeta) d\zeta, \quad (2)$$

where  $x$  denotes the coordinates outside the spiral unit,  $\zeta$  represents the coordinates on the boundary of the structure, and  $G_m$  indicates the Green's function of the material, satisfying the boundary conditions of continuity required by the Green's function.

Similarly, the eigenfunction  $\psi$  on the boundary  $\partial s$  is related to the total displacement  $x_i(\zeta) + x_{sc}(\zeta')$  by the Green's function,

$$\psi_n = - \oint_{\partial s} G^{-1}(\zeta, \zeta') [x_i(\zeta') + x_{sc}(\zeta')] d\zeta'. \quad (3)$$

Here,  $G$  is the Green's function inside the material, which satisfies the required continuity boundary conditions.  $G^{-1}$  is the inverse of the Green's function, satisfying the condition,

$$\int_s G^{-1}(x, x') G(x', x'') dx' = \delta(x, x''). \quad (4)$$

Substituting (4) into (3), the scattered field of the structure can be expressed as

$$\psi_{sc}(x) = \iint_{\partial s} G_m(x, \zeta) G^{-1}(\zeta, \zeta') [x_i(\zeta') + x_{sc}(\zeta')] d\zeta d\zeta'. \quad (5)$$

Equation (5) shows that the structural unit contributes to the surface response only in the direction  $G^{-1}(\zeta, \zeta')$ . On the structural surface  $\partial s$ , a set of orthogonal surface modes  $(\alpha, \beta)$  can be defined, and the structural surface response can be expressed as

$$G_{\alpha\beta} = \iint_{\partial s} \alpha^*(\zeta') G(\zeta, \zeta') \beta(\zeta) d\zeta d\zeta'. \quad (6)$$

By adjusting the unit structure, an ultimate scenario is achieved where the monopole  $G_+$  and dipole  $G_-$  responses reach equal amplitudes at a specific frequency. These two responses cancel each other out at the exit surface, preventing sound output and thereby achieving ultra-attenuation.

The total surface response of the metastructure can thus be described using the eigenmode expansion of the Green's function. Let  $Q_i$  represent the normalized eigenstates satisfying the continuity boundary conditions, and the Green's function can be expanded as

$$G(x', x) = \sum_i \frac{Q_i(x') Q_i^*(x)}{\rho_i(\omega_i^2 - \omega^2)}. \quad (7)$$

Here,  $\omega$  is the angular frequency, and  $\rho_i$  represents the average mass density of each eigenstate, defined as

$$\rho_i = \int_s Q_i^*(x) \rho(x) Q_i(x) dx, \quad (8)$$

where  $\rho(x)$  is the local mass density at point  $x$ .

For a high-aspect-ratio unit structure, its surface response can be expressed in terms of two components,

$$G_+ = \omega^2 \sum_i \frac{Q_i^*(h/2) [Q_i(h/2) + Q_i(-h/2)]}{(\omega_i^2 - \omega^2) \rho_i}, \quad (9)$$

$$G_- = \omega^2 \sum_i \frac{Q_i^*(h/2) [Q_i(h/2) - Q_i(-h/2)]}{(\omega_i^2 - \omega^2) \rho_i}. \quad (10)$$

Here,  $h/2$  and  $-h/2$  are the coordinates of the front and back surfaces of the spiral unit along the Z axis,  $Q_i(h/2)$  and  $Q_i(-h/2)$  correspond to the  $i$ th eigenmode of the structure, and  $Q_i^*(h/2)$  is its complex conjugate.

The total surface response for the periodic structure is

$$G(r, r') = \sum_i \sum_n c_n \psi_n(r) \psi_n^*(r'), \quad (11)$$

where  $i$  is the number of spiral units. For the problem we want to study, we are more concerned about the sound pressure attenuation after the sound wave passes through the structure. Therefore, the eigenfunction we need is the sound pressure distribution function, that is,  $\psi_n(r) = p_n(r)$ . Since the propagation of sound waves in structures is complex and obtaining an analytical expression is challenging, this study employs finite element numerical calculations to analyze the sound pressure attenuation. The semi-analytical formula for the sound absorption coefficient of the spiral metasurface,

derived by combining numerical results with analytical expressions, will be the focus of our next step. This work aims to fully leverage computational resources to reduce engineering manufacturing costs. By prioritizing simulation and analytical analysis to determine optimal parameters, the cost of large-scale experimental trials can be significantly reduced. The results are shown in Figs. 1(c) and 1(d).

### III. FEM MODELING METHOD

#### A. Structural and parameters

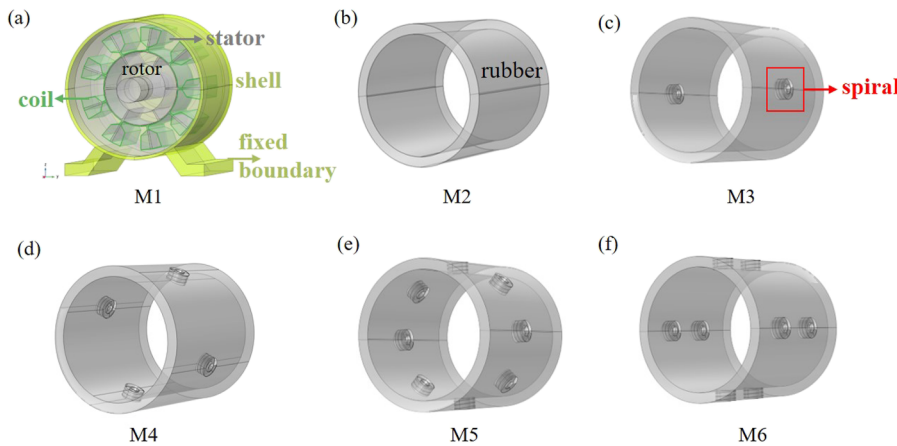
As shown in Fig. 2, the damping rubber embedded spiral metasurface (RSM) covering layer is generated by hollowing out a small circular hole in a cylindrical damping rubber with a thickness of 10 mm and the same size as the motor diameter and then embedding the spiral metasurface in the circular hole. The parameters that control the performance are mainly the pitch  $p$  and the total height  $h$  of the spiral unit (i.e., the rubber thickness). The medium of the entire calculation domain is air, and the relevant parameters of the motor, RSM, and background medium are shown in Table I.

Figure 2 is a schematic diagram of the motor model and various vibration and noise reduction treatments. First, we fill the outside of the motor with a layer of 10 mm rubber to perform traditional vibration and noise reduction treatment. Then, we use rubber as the base, hollow it out, and place  $n$  spiral metasurface units in the center. The motor model is a permanent magnet synchronous motor. Since the vibration and noise reduction structure does not depend on the motor's working conditions, there are no special requirements for the selection of the motor type.

Figure 2(a) shows the permanent magnet synchronous motor model. The gray parts are the rotor and stator, the green wireframe is marked as the coil, and the outermost yellow-green structure is the motor housing and bracket. The motor model can be found in the COMSOL case library. The goal of this article is not to study the operation and structure of the motor, so the motor model will not be described in detail. The entire motor model is fixed in space by the bottom boundary, and the boundary load is calculated from the electromagnetic effect of the rotor part. In the frequency response finite element analysis of all models, all boundary conditions and loading conditions are consistent. Figure 2(b) shows the motor case filled with pure damping rubber. Figures 2(c)–2(f) show the composite structure filled with damping rubber and a spiral metasurface. In order to reduce the vibration and noise of the motor, the motor shell is replaced by rubber and a spiral metasurface.

The replacement shell is placed outside the motor, with a thickness of 10 mm and an axial length of 145 mm. The mechanical excitation generated by the electromagnetic excitation and rotor movement inside the motor acts as a vibration noise source on the motor casing. The vibration of the motor casing generates radiation noise. The combined structure of damping rubber and a spiral metasurface covers the surface of the motor to reduce vibration and noise.

This structure is equivalent to applying a shock absorber on the surface of the motor while simultaneously embedding a sound-absorbing structure inside the shock absorber, representing a passive vibration and noise reduction method. Figure 3 shows a schematic diagram of the model through the shock absorber. The internal



**FIG. 2.** Model diagrams of different vibration reduction and noise reduction methods for motors. (a) Motor model without vibration and noise reduction treatment, (b) motor model filled with damping rubber, (c) motor model embedded with two spiral metasurfaces, (d) motor model embedded with four spiral metasurfaces, (e) model embedded with eight spiral metasurfaces in a single row, and (f) model embedded with eight spiral metasurfaces in two rows.

**TABLE I.** Relevant parameters of the motor, RSM, and background medium.

Parameter name	Value
Media name	Air
Medium density	1.29 (kg/m <sup>3</sup> )
Rubber density	1100 (kg/m <sup>3</sup> )
Rubber thickness	10 mm
Pitch	0.5 mm
Spiral path thickness	2 mm
Spiral path width	1.2 mm
Damping coefficient	0.7

vibrations and electromagnetic excitations of the motor are output as vibration noise sources. Through the composite structure of damping rubber and a spiral metasurface, the vibration amplitude of the motor is first dampened at the rubber. Simultaneously,

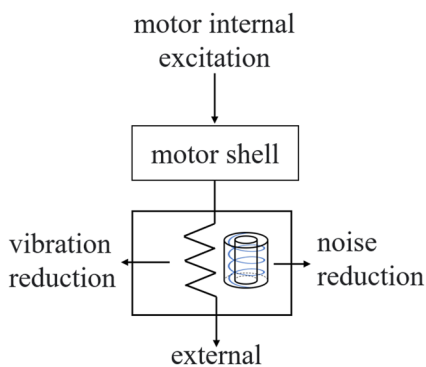


**FIG. 3.** Model schematic of motor vibration reduction and noise reduction. Internal electromagnetic and mechanical excitations in the motor propagate as vibration noise sources to the motor casing, which then radiates noise outward. Embedding damping rubber with spiral metasurfaces is akin to applying a layer of damping rubber on the outside of the motor casing for vibration reduction, while the spiral metasurfaces absorb sound, ultimately achieving attenuation of both vibration and noise.

the outwardly radiated noise enters the spiral structure. Due to the complexity of the spiral path, the sound waves undergo repeated refraction and reflection until their energy is attenuated.

Motor noise sources mainly come from electromagnetic excitation and mechanical excitation. Each of these sources belongs to the local characteristics of the motor system and has its own specific response to excitation under any working conditions. Therefore, traditional motor vibration and noise reduction measures mainly focus on optimizing the motor’s internal structure.<sup>42</sup> However, these tasks often require a large amount of computing resources and are highly specialized. They require different optimizations for different motors and are difficult to apply flexibly. In addition, as the requirements for motor performance become more stringent, the internal structure becomes correspondingly more complex, making it more challenging for traditional methods to achieve universal vibration and noise reduction. Therefore, it is necessary and urgent to design a universal, flexible, and adjustable method for motor vibration and noise reduction. Based on the above-mentioned considerations, and given the small size and unique performance characteristics of acoustic metasurfaces, this article proposes new ideas for applying acoustic metasurfaces to motor vibration and noise reduction.

According to the absorption characteristics of the spiral periodic structure in free space discussed in Sec. II, it can be seen that the ultra-wideband sound absorption efficiency of this structure is very significant, demonstrating its application potential in small machinery. Therefore, this section focuses on the analysis and research of applying the spiral metasurface structure to motor vibration and noise reduction.

**B. FEM simulation setup**

First, the electromagnetic force is calculated by simulating the 2D cross-sectional model of the motor. The rotating domain feature is used to rotate the rotor, and the electromagnetic force is then calculated using the force calculation feature in the magnetic field module. The “Weak Form Boundary PDE” module is used to store the electromagnetic force on the interface and to generate the FFT of these forces. The electromagnetic analysis study includes two steps: steady-state analysis and transient analysis. The steady-state analysis is used to initialize the electromagnetic field,

09 May 2025 02:44:09

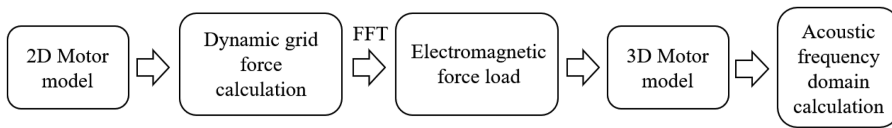


FIG. 4. Flow chart of the numerical computation.

while the transient analysis is used to solve for the electromagnetic force.

Next, the 2D motor model is extended to 3D. The calculated electromagnetic force is applied to the motor as an electromagnetic load using the boundary load feature. The motor vibrates and radiates noise outward. This part uses the structural finite element method to obtain the vibration characteristics of the motor and then uses the pressure acoustics module to perform frequency domain calculations to obtain sound pressure levels and other acoustic characteristics. Figure 4 shows the flow chart of the numerical computation.

#### IV. RESULTS AND DISCUSSION

First, using COMSOL for multiphysics simulation, the transient force calculation of the magnetic field is performed to compute the characteristic electromagnetic forces of a two-dimensional motor cross section. Subsequently, FFT is employed to represent the electromagnetic forces in the frequency domain. This analysis yields the spatial distribution of the forces, and the solver performs a discrete Fourier transform on the time-dependent variables, resulting in a series of complex coefficients. These forces produce displacements within the structure, which in turn convert into sound pressure. Subsequently, the pressure acoustics module computes the sound pressure and vibration amplitude on the motor surface using the exterior field characteristics.

To visually compare the vibration and noise reduction effects of the spiral metasurfaces, Fig. 5 shows the local frequency band vibration and noise reduction effects for an untreated motor and two spiral unit models. Figure 5(a) presents the normalized vibration amplitude of the M1 and M3 models within the 100–2000 Hz frequency band. The results indicate that the structure embedded with two spiral metasurfaces can reduce the vibration peak value by 59, an attenuation rate that is difficult to achieve with other methods. This is because the RSM can be regarded as a mass-spring system. When the vibration frequency matches the natural frequency of the RSM, the system achieves resonant absorption of the vibration energy.

Figure 5(b) shows the average sound pressure curves on the motor surface for the M1 and M3 models within the 6 k to 20 kHz frequency band. The results indicate that the structure embedded with two spiral metasurfaces can reduce the sound pressure level by up to 13 dB, with an average attenuation of 9 dB, achieving ultra-wideband sound attenuation. Due to the presence of the spiral metasurface, RSM redistributes the phase and propagation path of sound waves from vibrational noise, causing certain frequencies of sound waves to cancel each other out. In addition, the spiral structure extends the effective propagation path of the sound waves, allowing more sound energy to be converted into other forms of energy through material friction and structural deformation within the structure, ultimately achieving ultra-wideband attenuation within the perfect sound absorption band.

Figure 5(c) is a schematic diagram of the motor's sound radiation at a frequency of 500 Hz. The figure shows that the motor's radiated sound pressure level is significantly reduced, from the original 80 dB to ~40 dB. This is because the presence of the spiral metasurface achieves impedance matching on the RSM surface through phase adjustment, reflecting part of the sound waves back into the RSM structure at the exit end, thereby reducing the energy of sound waves radiated outward.

Figure 6 shows the comparison of vibration deformation and sound pressure attenuation results between motor models M1 and M3 at 500 Hz. The results indicate that in the rubber model embedded with two spiral metasurfaces, both the vibration amplitude and radiated sound pressure of the motor are significantly suppressed.

#### V. PARAMETRIC STUDY

##### A. Parameter settings for different models

To achieve the purpose of reducing noise, there are a total of five processing methods (see Table II for details). Model M1 represents a motor without vibration and noise reduction treatment. M2 represents a processing method that is only filled with rubber, while M3, M4, M5, and M6 represent structures with spiral metasurfaces nested on damping rubber. The spiral metasurface numbers are 2, 4, 8, and 8, respectively, where M5 and M6 are distributed in one row and two rows, respectively. The filling method is full axial filling outside the motor shell.

##### B. Vibration amplitude reduction of different models

Figure 7 displays the calculation results of motor vibration amplitude attenuation, presenting the vibration deformation diagram of the motor model at a frequency of 500 Hz under various models (M1–M6). The examined frequency response bandwidth spans from 100 Hz to 20 kHz, with a frequency resolution of 200 Hz. The black wireframe represents the original shape of the motor, while the color represents the motor shell. As the vibration amplitude of the motor is minimal, we express the values as relative deformation, with a reference value of  $1 \times 10^{-7}$  m.

Figure 7(a) shows the vibration deformation of the motor without any vibration or noise reduction measures. The results indicate that, when no vibration damping measures are applied, the motor deforms significantly, creating a noticeable deformation gap between the original motor frame and the motor frame. Figure 7(b) illustrates the deformation diagram of the motor when only damping rubber is used. The results show that while the damping rubber has some inhibitory effect on motor vibration, the effect is not substantial.

Figure 7(c) shows the deformation diagram of the motor case filled with damping rubber and embedded with two spiral metasurface models. The results indicate that the vibration deformation of

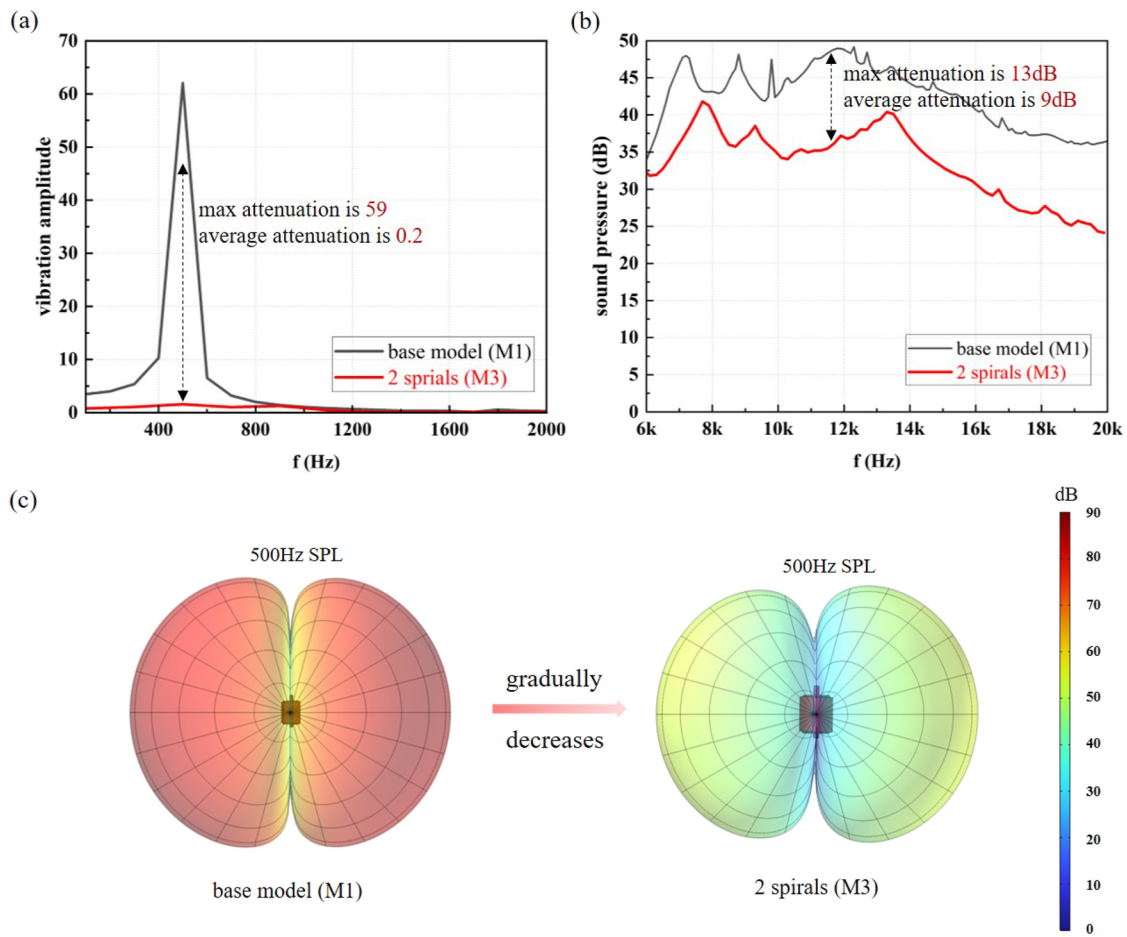


**FIG. 5.** Schematic diagram of the vibration and noise reduction efficiency in the local frequency band for the untreated motor (M1) and the model embedded with two spiral metasurfaces (M3). (a) Normalized vibration amplitude of the M1 and M3 models in the 100–2000 Hz frequency band, (b) average sound pressure distribution curves of the M1 and M3 models in the 6 k to 20 kHz frequency band, and (c) the comparison of sound radiation at 500 Hz for motor models M1 and M3.

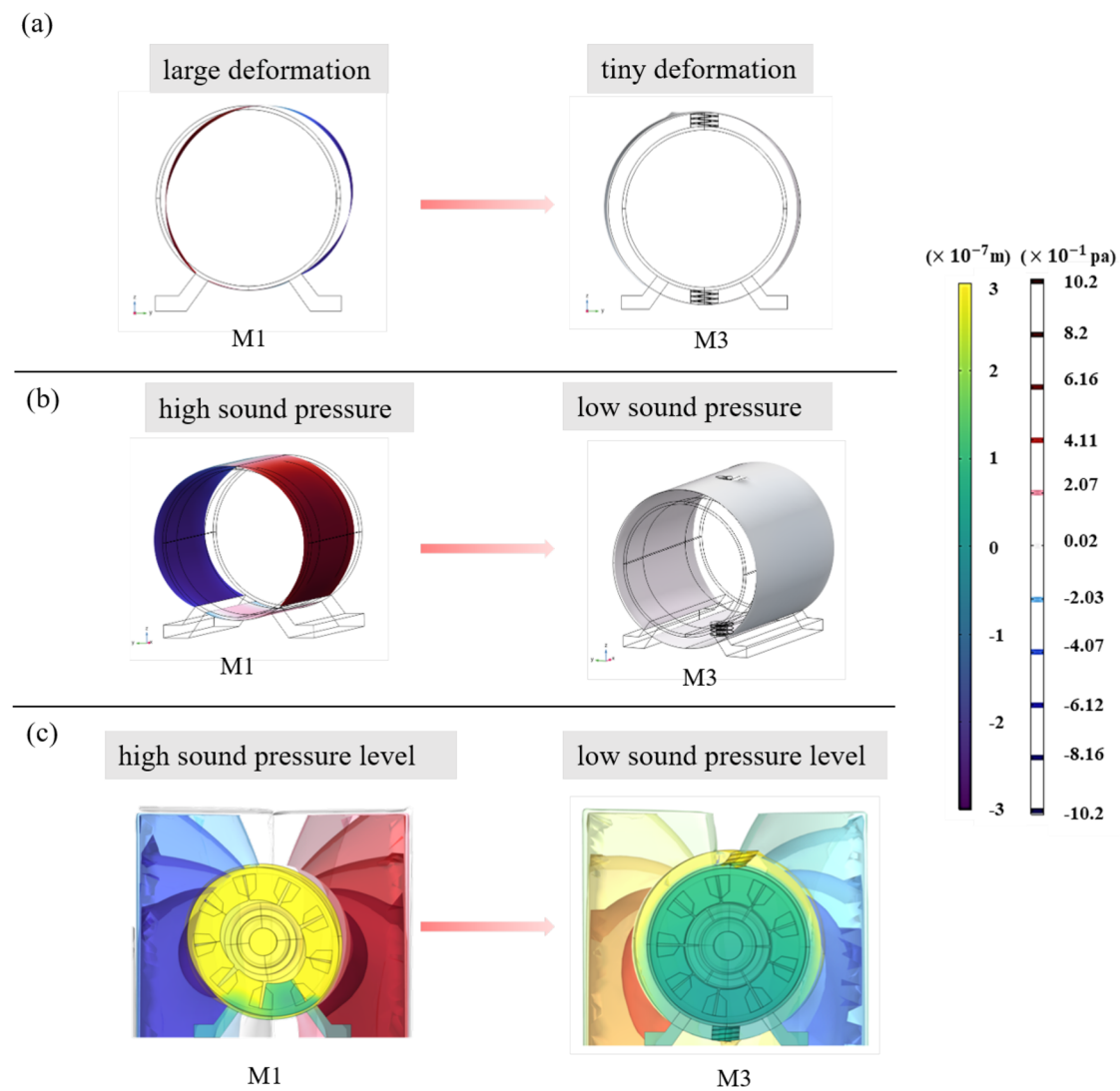
the motor has been significantly improved and has almost not deviated from the original motor position, though there is still a small amount of offset. Figures 7(d)–7(f), respectively, represent models with 4 and 8 embedded spiral metasurfaces. The results demonstrate that the motor shell shows almost no deflection, with deformation being significantly suppressed. This result demonstrates the excellent performance of spiral metasurfaces in motor vibration and noise reduction applications.

Table III shows the statistics of the simulation results of motor vibration reduction efficiency with different processing methods. The results show that damping rubber alone can inhibit motor vibration, but the proportion of attenuation frequency is 96%, and the average attenuation is only 0.69. The embedded spiral metasurface method can increase the attenuation ratio to 99%, and the average attenuation is increased to 0.99. The overall maximum attenuation does not show a significant difference.

Figure 8 shows the average normalized amplitude curves of different motor model surfaces. For clarity, the vibration peaks are marked in red in the figure. The results indicate that the original motor vibration peak can reach 62, while the rubber-filled model can reduce the peak to 22. The model embedded with the spiral metasurface can reduce the vibration peak by an order of magnitude, making the peak value only about 1.5. These results demonstrate that the vibration reduction efficiency of a single damping rubber is low, while the spiral metasurface exhibits superior performance in significantly improving vibration reduction efficiency.

### C. Sound absorption efficiency of different models

Figure 9 shows the calculated sound pressure distribution on the motor shell for different motor models at a frequency of 500 Hz. It corresponds one-to-one with the deformation results in Fig. 7



**FIG. 6.** Vibration and noise reduction efficiency diagrams of the untreated motor (M1) and the model embedded with two spiral metasurfaces (M3) at 500 Hz. (a) Comparison of vibration deformation between motor models M1 and M3 at 500 Hz, (b) comparison of sound pressure values between motor models M1 and M3 at 500 Hz, and (c) comparison of radiated sound pressure levels between motor models M1 and M3 at 500 Hz.

under the same conditions. The black wireframe represents the original shape of the motor, and the colors indicate the motor shell. The colors from dark to light show that the sound pressure distribution on the motor surface gradually decreases. The darkest red represents 2.5 Pa, the area close to white is almost 0 Pa, and blue represents the minimum value of  $-2.5$  Pa, with the negative sign indicating that the sound pressure phase is opposite to the reference direction.

Figure 9(a) shows the sound pressure distribution on the surface of the motor without any vibration and noise reduction measures. The results indicate that when no vibration damping measures are applied, the sound pressure distribution value on the surface of the motor is relatively large, close to the maximum value except for

the base part of the motor. Figure 9(b) shows the sound pressure distribution on the motor surface when only damping rubber is used. The results indicate that the damping rubber has a certain attenuation effect on the motor radiation noise, but it is not significant and remains around 2.3 Pa.

Figures 9(c)–9(f) show the sound pressure distribution diagrams of the motor case filled with damping rubber and embedded with 2, 4, 8, and  $2 \times 4$  spiral metasurface models. The results demonstrate that the motor radiation noise is significantly reduced, almost to zero. Among these, M5 and M6 represent models with 8 spiral metasurfaces embedded, but with different embedding methods. M5 represents a uniform arrangement in one row along the perimeter,

**TABLE II.** Different vibration damping and noise reduction methods: parameter statistics. M1–M6 represent the model numbers of different vibration damping and noise reduction methods.

Model number	Rubber filling position	Number of spiral metasurfaces
M1	No	0
M2	Full axial filling	0
M3	Full axial filling	2
M4	Full axial filling	4
M5	Full axial filling (one line)	8
M6	Full axial filling (two lines)	8

while M6 represents a uniform arrangement in two rows. The results of the two arrangements are different. The sound pressure distribution of M5 is slightly larger than that of M6, indicating that the one-row arrangement is not suitable for motor noise reduction.

To quantitatively compare the vibration and noise reduction efficiency of each model, we measured the average vibration amplitude and average sound pressure level of the motor surface for each model. We focused on the maximum attenuation degree, average attenuation degree, and the proportion of vibration attenuation frequency within the bandwidth of interest produced by different processing methods in motor vibration and noise reduction. The results are shown in Figs. 8 and 10, and the comparison results are listed in Tables III and IV.

Table IV shows the statistics of the simulation results of motor sound attenuation efficiency with different processing methods. The results indicate that the layouts of M3, M4, and M6 are notably superior, with an attenuation ratio of 82% and above. While M6 exhibits the highest maximum attenuation sound pressure level, its average attenuation sound pressure level is not as good as M4. In a comprehensive comparison, M3 demonstrates the best performance,

**TABLE III.** Vibration reduction efficiency simulation results of different vibration reduction and noise reduction treatment methods.

Model code	Proportion of vibration attenuation frequency (%)	Maximum degree of attenuation	Average degree of attenuation
M2	96	61.66	0.69
M3	99	60.82	0.99
M4	99	60.76	0.99
M5	99	60.68	0.99
M6	99	60.67	0.99

requiring the smallest construction resources and engineering manufacturing complexity. However, its average attenuation is only 0.4 dB lower than M4, and the maximum attenuation value is only 6.3 dB lower. Therefore, the method of embedding two spiral metasurfaces fully meets the requirements for vibration and noise reduction in motors without the need for more complex quantity accumulation. The rubber filling method can achieve 76% sound attenuation, but its maximum attenuation value is only 12.3 dB, and its average attenuation is only 4.5 dB.

The results indicate that the rubber filling method alone is not efficient for vibration and noise reduction in motors. The M5 model achieves only a 29% reduction in sound pressure, with a maximum sound attenuation of just 4 dB, and the average attenuation is negative. This result indicates that the M5 model actually increases sound pressure and is therefore unsuitable for motor vibration and noise reduction. The calculations for M5 also show that there is a limit to the number of single-row spiral metasurfaces. When the number of spirals exceeds this limit, the vibration noise is amplified instead.

Figure 10 shows the average sound pressure distribution curves on the surfaces of different motor models. To facilitate comparison,

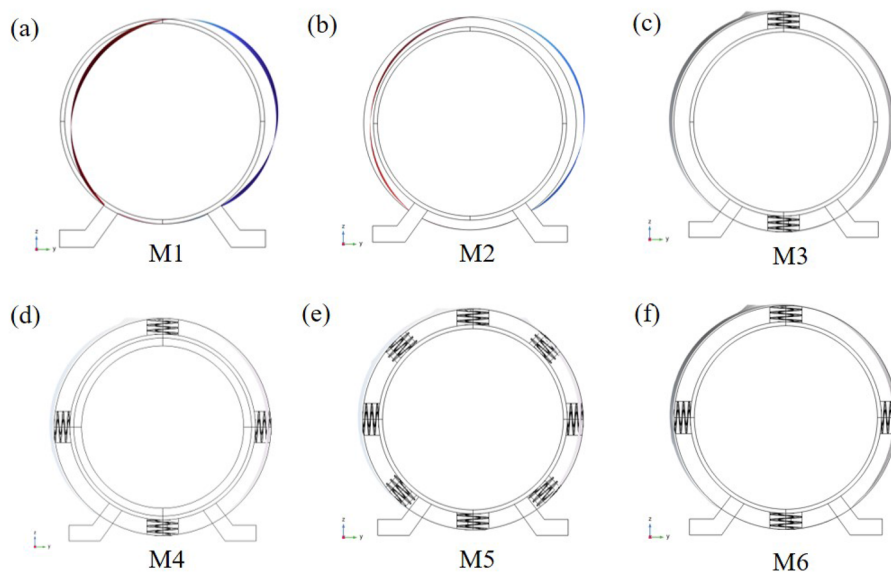


**FIG. 7.** Deformation diagrams of different motor models at the frequency of 500 Hz. (a) Motor model without vibration and noise reduction treatment, (b) motor model filled with damping rubber, (c) motor model embedded with two spiral metasurfaces, (d) motor model embedded with four spiral metasurfaces, (e) model embedded with eight spiral metasurfaces in a single row, and (f) model embedded with eight spiral metasurfaces in two rows.

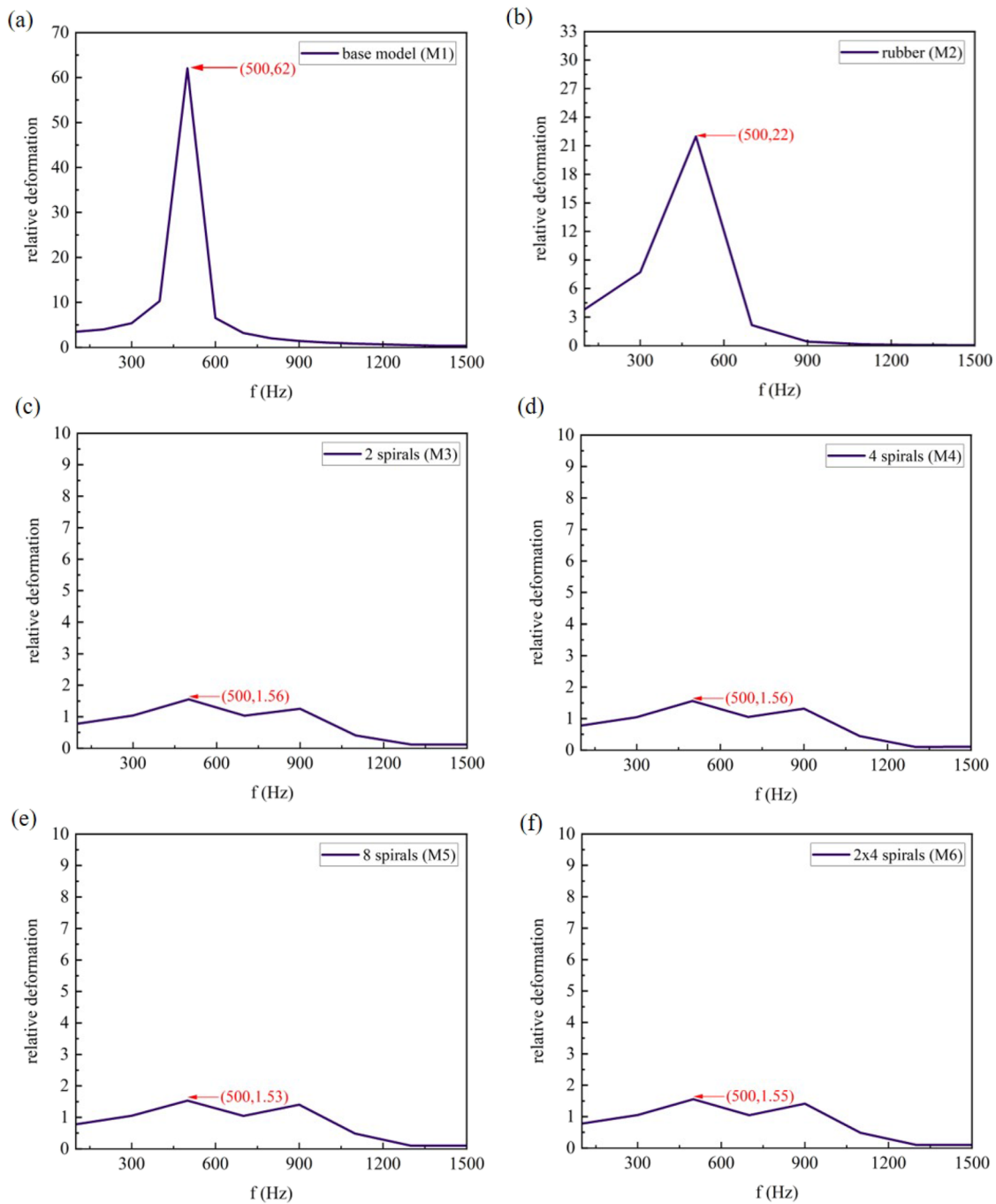


**FIG. 8.** Average normalized vibration amplitude of different motor model surfaces. The red mark is the frequency corresponding to the vibration peak. [(a)–(f)] Average vibration amplitude curves of the surfaces of models M1–M6.

the dotted line in the figure indicates the quieter sound pressure level, which is 30–40 dB. The results show that without any processing on the motor, most of the motor noise is above 40 dB, as shown in Fig. 10(a). Figure 10(b) shows that only filling the motor

with rubber can effectively reduce noise, but the reduction efficiency is limited and the effect is not obvious.

Figure 10(c) shows the result curve of embedding two spiral metasurfaces in the rubber layer. It can be seen that most of the noise

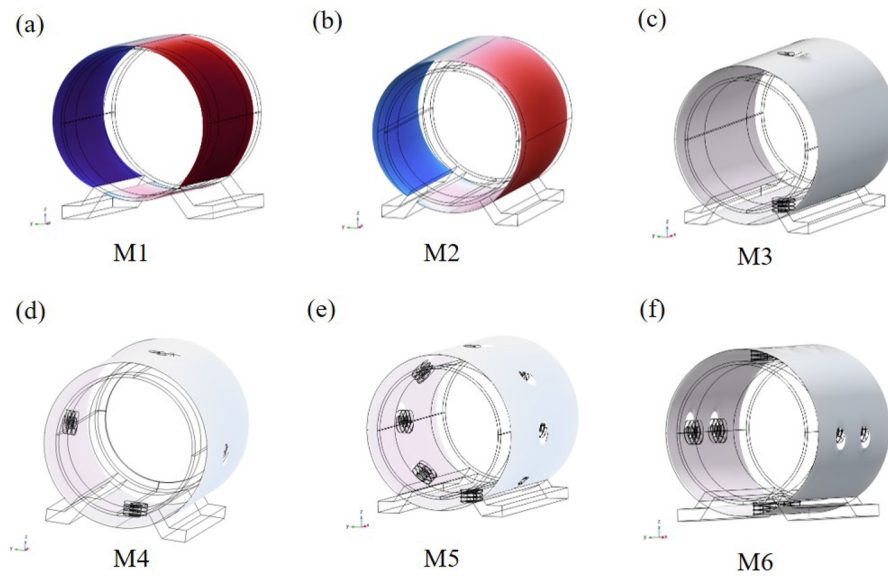


**FIG. 9.** Distribution of surface sound pressure values of different motor RSM models. [(a)–(f)] M1–M6 are heat maps of surface sound pressure value distribution of different RSM models.

can be reduced to less than 40 dB. Figure 10(d) shows the result curve of four spiral metasurfaces embedded in the rubber layer. The sound attenuation is better than that of two spirals, but the improvement effect is not obvious. Figures 10(e) and 10(f) show the result curve of eight spiral metasurfaces embedded in the rubber layer, with M5 arranged uniformly along the circumference in a single row.

The results show that the sound pressure is not attenuated but enhanced, indicating that in the case of a single-row arrangement, the number of units on the spiral metasurface has a limit. When this limit is exceeded, the sound attenuation function fails. M6 is the model calculation result of two rows of embedded spiral metasurfaces. The results show that the two rows of spiral metasurfaces still have the ability to attenuate sound, but the effect is not much enhanced compared to M4 and M3.

To sum up, when using the composite structure of a spiral metasurface and damping rubber for motor vibration and noise reduction, there is a limit to the number of embedded spiral metasurfaces. When this limit is exceeded, the efficiency of sound attenuation is no longer significantly improved. In this study, the optimal choice is two embedded spirals, as exceeding this number does not significantly improve the effect but doubles the engineering complexity, so there is no need to continue increasing the number.

#### D. Sound radiation sound pressure level attenuation of different models

Figure 11 shows the calculated results of radiation noise levels at 500 Hz for different motor models (M2, M4, M5, and M6). By comparing the results of the four figures, it is evident that ordinary rubber has a poor noise radiation attenuation effect on the motor, whereas embedding spiral metasurfaces in the rubber can significantly reduce the noise sound pressure level. In addition, this method has minimal dependence on the number of spirals,

meaning that only one or two spirals embedded in the rubber can achieve excellent results without complex quantity design.

Figure 12 shows the vibration amplitude and sound pressure isosurface maps for different motor models. In these figures, green and yellow values represent vibration amplitude (unit: meters), while red and blue represent sound pressure isosurfaces (unit: pascals). The more yellow there is, the greater the vibration amplitude, with green indicating almost zero vibration amplitude. Similarly, for the sound pressure isosurface map, colors closer to red indicate higher sound pressure, while colors closer to light blue indicate lower sound pressure.

Comparing the results shown, the motor without vibration and noise reduction treatment (M1) has vibration maps almost entirely yellow, indicating that the entire structure is vibrating intensely. Pure rubber filling (M2) can slightly reduce the vibration amplitude, but the effect is not significant. However, the method of embedding spiral metasurfaces in rubber (M3–M6) can greatly reduce the vibration amplitude. Similarly, the sound pressure isosurface values of the M1 and M2 motor models are much larger than those of the motors treated with spiral metasurfaces (M3–M6). This result indicates that embedding spiral metasurfaces in rubber can not only significantly reduce vibration but also effectively attenuate sound pressure.

Based on the above-mentioned results, it can be seen that for small structures such as motors, efficient vibration and noise reduction can be achieved by designing metasurfaces. The composite structure of damping rubber and spiral metasurface proposed in this article can cover the surface of the motor. While the damping rubber reduces vibration, the spiral metasurface structure absorbs the radiated noise into the interior for attenuation. This structure only needs to embed up to two spiral metasurfaces in the damping rubber to achieve ideal vibration and noise reduction effects, greatly simplifying the process difficulty and design complexity and providing great application value. At the same time, due to the multi-parameter adjustability of the spiral metasurface, any attenuation within the

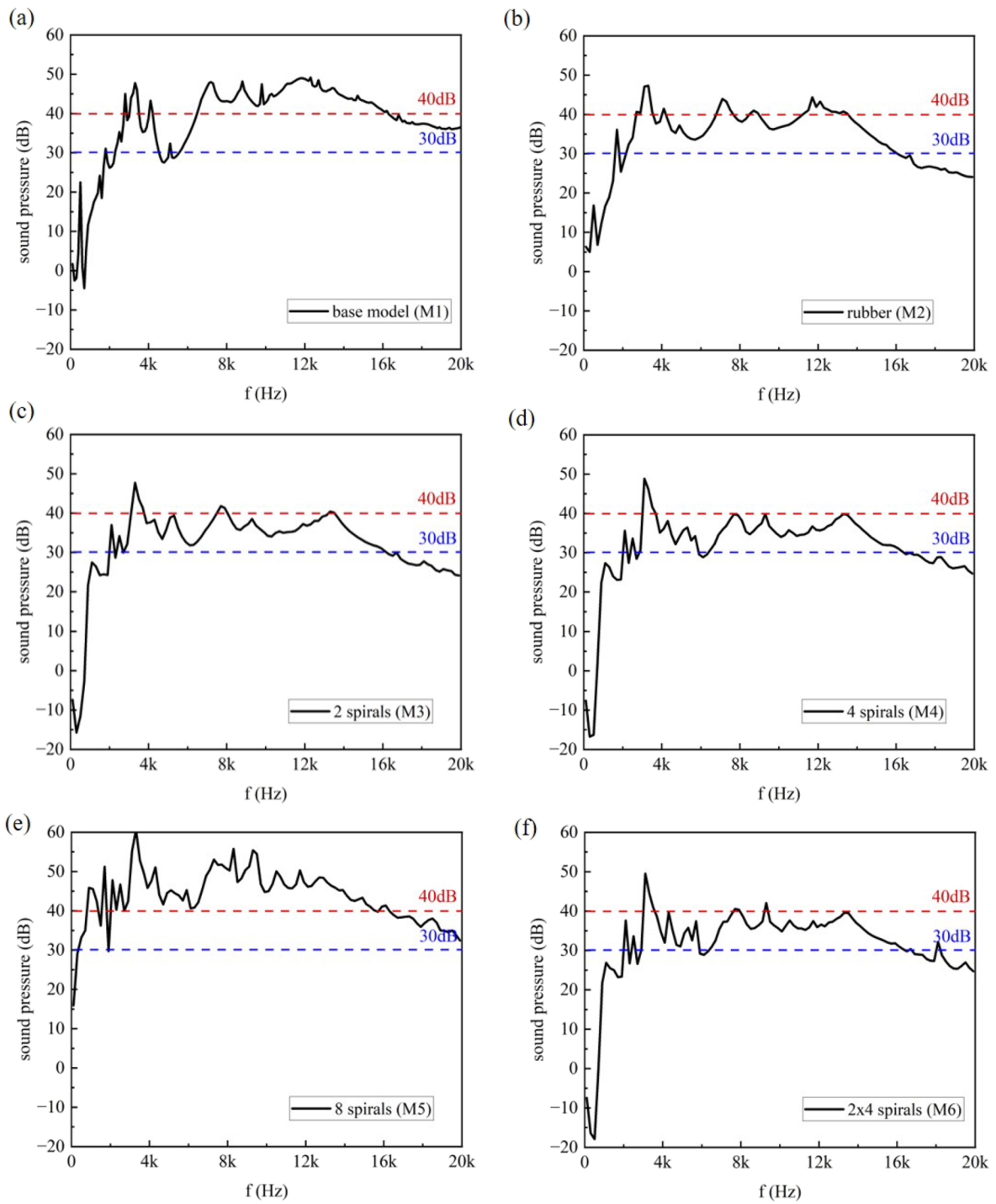


**FIG. 10.** Average sound pressure distribution curves on the surfaces of different motor models. The blue dotted line represents 30 dB, the red curve represents 40 dB, and the space between the two dotted lines represents the quieter reference sound pressure level range. [(a)–(f)] Average sound pressure distribution curves on the surfaces of models M1–M6.

09 May 2025 02:44:09

**TABLE IV.** Simulation results of sound attenuation efficiency of different vibration and noise reduction processing methods.

Model code	Proportion of vibration attenuation frequency (%)	Maximum degree of attenuation (dB)	Average degree of attenuation (dB)
M2	76	12.3	4.5
M3	82	34.1	6.2
M4	83	38.8	6.6
M5	29	4	-5.6
M6	82	40.4	6.5

target frequency band can be achieved by adjusting the structural parameters, providing flexible operability for practical applications. The work of this article also provides a basis for the research of smart metamaterials.

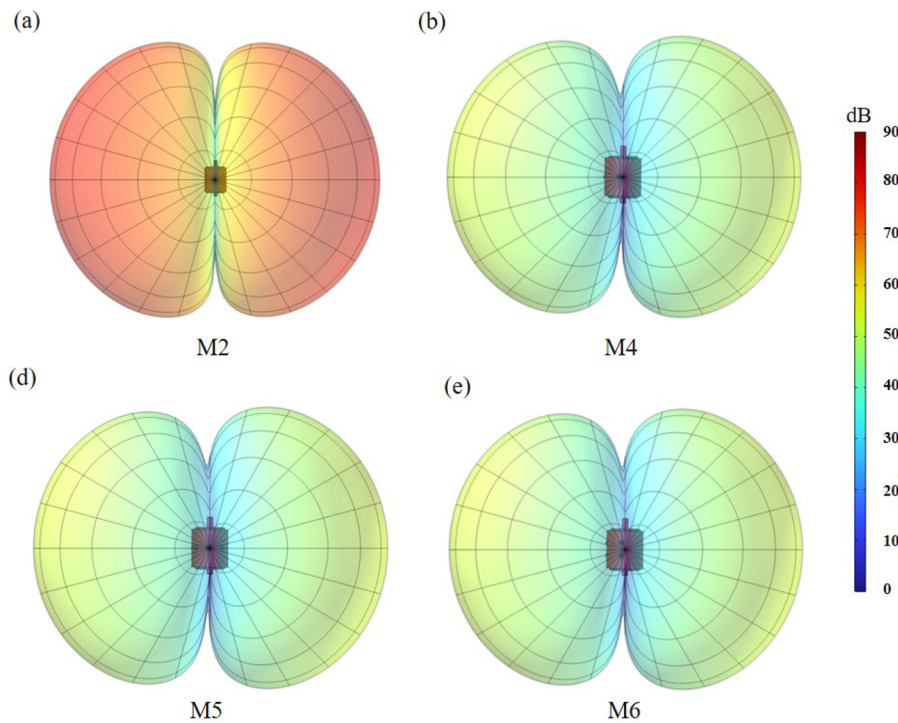
As mentioned earlier, for a specific target frequency band, the parameters of the helical metasurface have limit values. Therefore, it is necessary to design an optimization algorithm to efficiently calculate the optimal parameters for each working condition according to the specified goals. This can greatly save actual experimental resources and will be the focus of our next research phase. At the same time, most of the calculations in this article are finite element calculations, which are not very efficient. For vibration and noise

problems, it is very feasible to use boundary elements to improve efficiency. Therefore, our next step is to design a set of boundary elements based on the performance of the spiral metasurface. The automatic optimization program of the meta-algorithm provides a large amount of accurate prior data for practical applications and saves actual costs.

### E. Future outlook

In practical applications, the alignment between the motor and the load plays a crucial role in the mechanical operation's precision. Due to the potential deformation or local displacement caused by the helical metamaterial structure, the traditional rigid connection between the motor and the shaft may not maintain ideal alignment, thereby affecting the system's stability and performance. To address this issue, we will consider using flexible couplings to connect the motor and the load shaft in future applications. These couplings, through their elastic structure, provide a certain degree of adaptability, allowing them to absorb small displacements and vibrations between the shafts, thereby reducing the mechanical stress caused by alignment errors.

Another point to consider is that, in practical applications, the metal helical structure may experience fatigue under repeated compression, which could affect its long-term performance and reliability. In future engineering applications, we will consider optimizing material selection and other measures to enhance the fatigue resistance of the helical structure.

**FIG. 11.** Radiated noise plots of the motor for different vibration and noise reduction models. [(a)–(d)] Radiated noise sound pressure levels for models M2 and M4–M6, in dB.

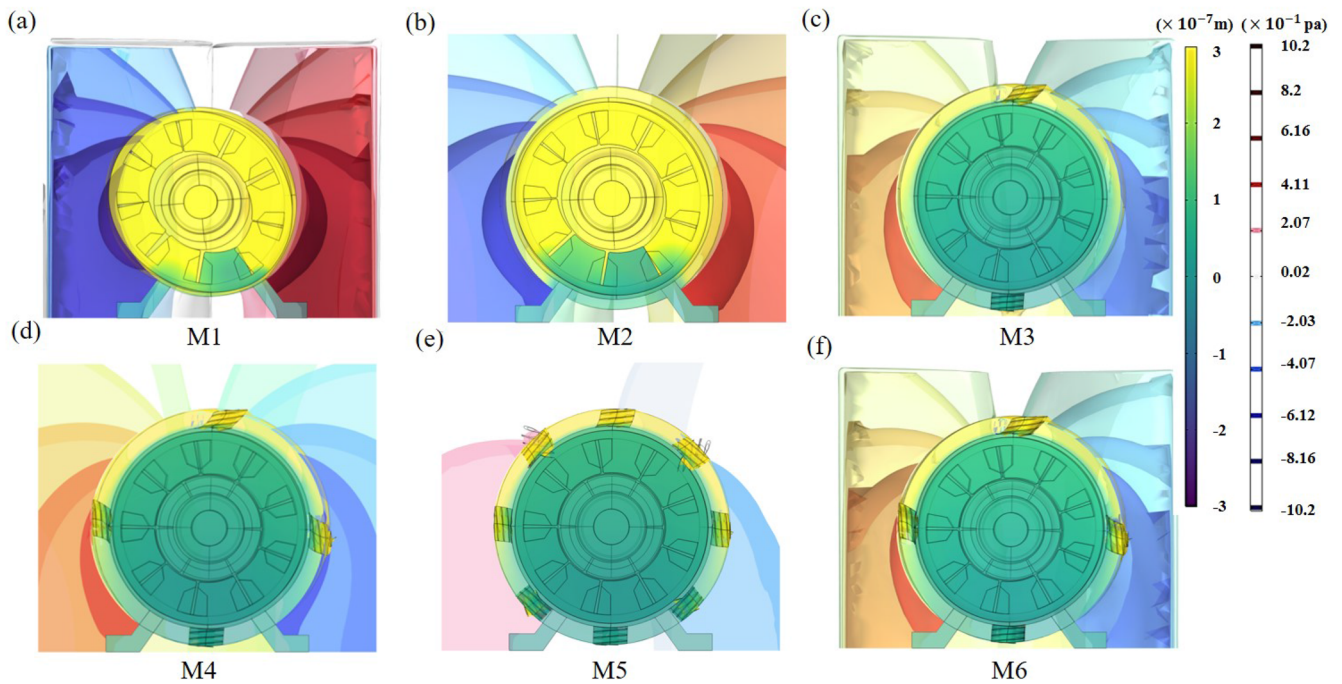


**FIG. 12.** Vibration amplitude and sound pressure isosurface maps for different motor models. [(a)–(f)] The vibration amplitude and sound pressure isosurface maps for motor models M1–M6, green and yellow values represent vibration amplitude (unit: meters), while red and blue represent sound pressure isosurfaces (unit: pascals).

## VI. SUMMARY AND CONCLUSIONS

In this article, we presented a vibration and noise reduction structure with a spiral metasurface embedded in the base of damping rubber. Using a permanent magnet synchronous motor as a model, we analyzed its vibration and noise reduction efficiency. Detailed numerical simulation models were employed to verify the superior performance of this composite structure. The damping rubber-embedded spiral metasurface structure consists of a hollowed-out cylinder and a spiral path. The entire structure is equivalent to a shock absorber plus a sound absorber. The structural vibration is suppressed by the damping rubber, and the radiated noise is absorbed by the spiral metasurface. Sound waves undergo multiple refractions and reflections within the spiral metasurface until they reach an optimal attenuation level. This structural configuration yields impressive results, with 99% vibration attenuation and over 80% sound pressure attenuation. Moreover, the average sound pressure level attenuation surpasses 6.2 dB, effectively mitigating noise to quieter levels and achieving ultra-wideband attenuation. Compared to traditional narrow-band vibration and noise reduction methods for motors, these results show a significant decrease in both the bandwidth and amplitude of vibration and noise, thereby markedly improving performance. This research presents a flexible, multi-parameter adjustable structure for vibration and noise reduction in small motor-type devices, independent of the internal operating conditions of the device. It has the potential to offer general vibration and noise reduction solutions for motors while also providing a data foundation for intelligent structural design aimed

at vibration reduction. The next step will involve manufacturing and experimental work based on the results presented in this article. However, due to the complexity of the motor structure and the metasurface mechanism, it is difficult to obtain accurate expressions relying solely on analytical analysis. We will first combine simulation data for big data analysis and design an automated optimization algorithm, followed by experimental validation based on the optimal structural parameters. These extensions are left for future work.

## ACKNOWLEDGMENTS

The work reported in this article was supported by the National Natural Science Foundation of China (Grant No. 12372198).

## AUTHOR DECLARATIONS

### Conflict of Interest

The authors have no conflicts to disclose.

## Author Contributions

**Huilan Wu:** Data curation (equal); Methodology (equal); Writing – original draft (equal). **Han Zhang:** Validation (equal); Writing – review & editing (equal). **Yijun Liu:** Funding acquisition (equal); Writing – review & editing (equal).

## DATA AVAILABILITY

The data that support the findings of this study are available from the corresponding authors upon reasonable request.

## REFERENCES

- <sup>1</sup>W. Cai, X. Wu, M. Zhou, Y. Liang, and Y. Wang, "Review and development of electric motor systems and electric powertrains for new energy vehicles," *Autom. Innov.* **4**, 3 (2021).
- <sup>2</sup>S. Li and W. Xu, "Vibration analysis of permanent magnet synchronous motor using coupled finite element analysis and optimized meshless method," *Nonlinear Dyn.* **108**, 167–189 (2022).
- <sup>3</sup>P. Saiteja and B. Ashok, "Experimental investigation of vibro-acoustic noise analysis in the switched reluctance motor through transient model-based multiphysics analysis for electric vehicles applications," *Appl. Acoust.* **220**, 109957 (2024).
- <sup>4</sup>C. M. Harris and A. G. Piersol, *Harris' Shock and Vibration Handbook* (McGraw-Hill, NY, 2002), Vol. 5.
- <sup>5</sup>H.-s. Kim and B.-i. Kwon, "Optimal design of motor shape and magnetisation direction to obtain vibration reduction and average torque improvement in IPM BLDC motor," *IET Electr. Power Appl.* **11**, 378–385 (2017).
- <sup>6</sup>K. Bo, J. Chen, Y. Jiang, and D. Wang, "Numerical analysis of 40 MW HTS motor electromagnetic characteristics for ship electric propulsion," *Sci. Rep.* **13**, 20261 (2023).
- <sup>7</sup>H. Phan, P. N. Hoa, H. A. Tam, P. D. Thang, and N. H. Duc, "Multi-directional triboelectric nanogenerator based on industrial Q-switched pulsed laser etched aluminum film," *Extreme Mech. Lett.* **40**, 100886 (2020).
- <sup>8</sup>M. L. Latash, *Fundamentals of Motor Control* (Academic Press, 2012).
- <sup>9</sup>W. Sun, Y. Li, J. Huang, and N. Zhang, "Vibration effect and control of in-wheel switched reluctance motor for electric vehicle," *J. Sound Vib.* **338**, 105–120 (2015).
- <sup>10</sup>F. Lin, S.-G. Zuo, W.-Z. Deng, and S.-L. Wu, "Reduction of vibration and acoustic noise in permanent magnet synchronous motor by optimizing magnetic forces," *J. Sound Vib.* **429**, 193–205 (2018).
- <sup>11</sup>S. Zuo, F. Lin, and X. Wu, "Noise analysis, calculation, and reduction of external rotor permanent-magnet synchronous motor," *IEEE Trans. Ind. Electron.* **62**, 6204–6212 (2015).
- <sup>12</sup>T. Sun, J.-M. Kim, G.-H. Lee, J.-P. Hong, and M.-R. Choi, "Effect of pole and slot combination on noise and vibration in permanent magnet synchronous motor," *IEEE Trans. Magn.* **47**, 1038–1041 (2011).
- <sup>13</sup>S. Wang and H. Li, "Reduction of electromagnetic vibration and noise in permanent magnet motor for EVs by optimizing design of rotor based on GPR-PSO model," *J. Electr. Eng. Technol.* **15**, 1231–1243 (2020).
- <sup>14</sup>S. He, P. Zhang, M. Muir, and B. Koch, "Rotor optimization to reduce electric motor noise," *SAE Int. J. Adv. Curr. Pract. Mobility* **6**, 39–47 (2023).
- <sup>15</sup>Y. Zhu, A. Merkel, K. Donda, S. Fan, L. Cao, and B. Assouar, "Nonlocal acoustic metasurface for ultrabroadband sound absorption," *Phys. Rev. B* **103**, 064102 (2021).
- <sup>16</sup>X. Jiang, B. Liang, X.-y. Zou, J. Yang, L.-l. Yin, J. Yang, and J.-c. Cheng, "Acoustic one-way metasurfaces: Asymmetric phase modulation of sound by subwavelength layer," *Sci. Rep.* **6**, 28023 (2016).
- <sup>17</sup>Y. Cheng, C. Zhou, B. G. Yuan, D. J. Wu, Q. Wei, and X. J. Liu, "Ultra-sparse metasurface for high reflection of low-frequency sound based on artificial Mie resonances," *Nat. Mater.* **14**, 1013–1019 (2015).
- <sup>18</sup>T. Zhao, Y. Li, L. Zuo, and K. Zhang, "Machine-learning optimized method for regional control of sound fields," *Extreme Mech. Lett.* **45**, 101297 (2021).
- <sup>19</sup>E. Rohan and V. Lukeš, "Homogenization of the vibro-acoustic transmission on periodically perforated elastic plates with arrays of resonators," *Appl. Math. Modell.* **111**, 201–227 (2022).
- <sup>20</sup>H. Long, C. Shao, C. Liu, Y. Cheng, and X. Liu, "Broadband near-perfect absorption of low-frequency sound by subwavelength metasurface," *Appl. Phys. Lett.* **115**, 103503 (2019).
- <sup>21</sup>K. Li, X. Zhang, J. Rong, J. Zhang, and N. Hu, "Broadband metasurfaces for steering flexural waves in thin plates: A topology optimization approach," *Appl. Acoust.* **221**, 110042 (2024).
- <sup>22</sup>J. H. Park, Y. Y. Kim, P. S. Ma, and J. S. Lee, "Broad and sharp-transient sound absorption band in phase-gradient metasurface lined with thin porous layer," *Appl. Acoust.* **218**, 109884 (2024).
- <sup>23</sup>H. Zhang, Q. Wang, M. Fink, and G. Ma, "Optimizing multi-user indoor sound communications with acoustic reconfigurable metasurfaces," *Nat. Commun.* **15**, 1270 (2024).
- <sup>24</sup>Y. Shen, P. Jiang, F. Liu, Y. Xu, and Z. Yang, "Flexural edge waves and customizable local modes of circular plates with metasurface," *Appl. Math. Modell.* **138**, 115749 (2025).
- <sup>25</sup>T. Liang, M. He, H.-W. Dong, L. Xia, and X. Huang, "Ultrathin waterborne acoustic metasurface for uniform diffuse reflections," *Mech. Syst. Signal Process.* **192**, 110226 (2023).
- <sup>26</sup>H. Long, C. Liu, C. Shao, Y. Cheng, K. Chen, X. Qiu, and X. Liu, "Subwavelength broadband sound absorber based on a composite metasurface," *Sci. Rep.* **10**, 13823 (2020).
- <sup>27</sup>H. Ryoo and W. Jeon, "Perfect sound absorption of ultra-thin metasurface based on hybrid resonance and space-coiling," *Appl. Phys. Lett.* **113**, 121903 (2018).
- <sup>28</sup>Z. Tian, Y. Meng, S. Zhao, Y. Wang, and Z. Chang, "Moth-wing-inspired metasurface for modulating sound amplitude and phase," *Mech. Syst. Signal Process.* **223**, 111849 (2025).
- <sup>29</sup>G. Palma, H. Mao, L. Burghignoli, P. Göransson, and U. Iemma, "Acoustic metamaterials in aeronautics," *Appl. Sci.* **8**, 971 (2018).
- <sup>30</sup>G. Wang, B. Ma, W. Yuan, and J. Luo, "Microperforated metasurface panel backed by aerogel-filled cavities for broadband low frequency sound absorption," *Appl. Acoust.* **208**, 109377 (2023).
- <sup>31</sup>S. Kumar and H. Lee, "The present and future role of acoustic metamaterials for architectural and urban noise mitigations," *Acoustics* **1**, 590–607 (2019).
- <sup>32</sup>Y. Liu, W. Zhang, G. Cao, G. Zuo, C. Liu, and F. Ma, "Ultra-thin ventilated metasurface pipeline coating for broadband noise reduction," *Thin-Walled Struct.* **200**, 111916 (2024).
- <sup>33</sup>B.-I. Popa, Y. Zhai, and H.-S. Kwon, "Broadband sound barriers with bianisotropic metasurfaces," *Nat. Commun.* **9**, 5299 (2018).
- <sup>34</sup>H.-T. Zhou, W.-X. Fu, X.-S. Li, Y.-F. Wang, and Y.-S. Wang, "Loosely coupled reflective impedance metasurfaces: Precise manipulation of waterborne sound by topology optimization," *Mech. Syst. Signal Process.* **177**, 109228 (2022).
- <sup>35</sup>Y. Ou and Y. Zhao, "On enhancing the noise-reduction performance of the acoustic lined duct utilizing the phase-modulating metasurface," *Sci. Rep.* **13**, 22184 (2023).
- <sup>36</sup>N. Gao, Z. Zhang, Y. Li, and G. Pan, "Experimental verification of ultra-broadband vibration reduction of underwater vehicle pressure-resisting shells using acoustic black holes," *Thin-Walled Struct.* **211**, 113118 (2025).
- <sup>37</sup>J. Deng, N. Gao, X. Chen, B. Han, and H. Ji, "Evanescence waves in a metabeam attached with lossy acoustic black hole pillars," *Mech. Syst. Signal Process.* **191**, 110182 (2023).
- <sup>38</sup>H. Wu, H. Zhang, and C. Hao, "Reconfigurable spiral underwater sound-absorbing metasurfaces," *Extreme Mech. Lett.* **47**, 101361 (2021).
- <sup>39</sup>H. Wu, C. Hao, and H. Zhang, "Underwater broadband sound insulation with chiral spiral structures," *AIP Adv.* **10**, 125022 (2020).
- <sup>40</sup>M. Sun, X. Fang, D. Mao, X. Wang, and Y. Li, "Broadband acoustic ventilation barriers," *Phys. Rev. Appl.* **13**, 044028 (2020).
- <sup>41</sup>M. Yang, G. Ma, Y. Wu, Z. Yang, and P. Sheng, "Homogenization scheme for acoustic metamaterials," *Phys. Rev. B* **89**, 064309 (2014).
- <sup>42</sup>J. Sun, "Research on vibration reduction, noise reduction and low torque ripple of switched reluctance motor," Ph.D. thesis, Huazhong University of Science and Technology, 2005.